

Role of cross-flow vibrations in the flow-induced rotations of an elastically mounted cylinder-plate system

Tao Tang^{1,2} (唐涛), Hongjun Zhu^{1,*} (朱红钧), Qing Xiao^{2,**} (肖清), Quanyu Chen¹ (陈泉宇),
Jiawen Zhong¹ (钟家文)

¹ State Key Laboratory of Oil and Gas Reservoir Geology and Exploitation, Southwest Petroleum University, Chengdu 610500, China

² Department of Naval Architecture, Ocean and Marine Engineering, University of Strathclyde, Glasgow, G4 0LZ, United Kingdom

*Corresponding author: zhuhj@swpu.edu.cn

**Corresponding author: qing.xiao@strath.ac.uk

Abstract:

Vibration and rotation represent two common fluid-structure-interaction phenomena, which can occur independently or concurrently. While extensive research has been conducted on individual vibration/rotation cases, there is relatively limited literature on coupled cases. However, it is crucial to recognize that coupled responses, such as those observed in falling leaves, are more prevalent in both natural occurrences and engineering scenarios. Hence, this study aims to investigate the influence of cross-flow vibrations on the flow-induced rotations of an elastically mounted cylinder-plate system. A broad range of rotational reduced velocities, spanning $U_\theta = 2-18$, is examined across four distinct vibrational reduced velocities, namely $U_y = 5, 8, 12, \text{ and } 18$. Numerical results indicated that a bifurcation phenomenon, wherein the cylinder-plate deflects to a non-zero equilibrium position, occurs at relatively high values of U_θ and U_y . Four distinct response modes have been identified: vibration-dominated, rotation-dominated, augmentation (VIV-like), and augmentation (galloping-like) mode. These response modes exert significant influence on phase angles between rotary angle and displacement as well as vortex shedding modes. In the rotation-dominated region, VIV-like region, and galloping-like region, phase angles exhibit a continuous decreasing trend, a consistent level of 180° and 90° , respectively. Transitions between vibration and rotation responses result in sharp increases in phase angles. The wake flow in the rotation-dominated mode and VIV-like mode demonstrates a 2S mode (two single vortices), while the vibration-dominated mode is characterized by a predominant 2T mode (two triplets of vortices). In the galloping-like region, large amplitudes lead to the increase in numbers of vortices, presenting 2S, 2S*, and 2P (two pairs of vortices) mode at $U_y = 8$, and 2P, P+S (one pair and one

single vortices) and 2P+S (two pairs and one single vortices) mode at $U_y = 12$, where the 2S* mode consists of two single vortices, each exhibiting a tendency to split into two smaller vortices as they migrate downwards. The mechanism behind the notable amplification of rotation/vibration responses is elucidated. Apart from the pressure difference induced by vortex shedding, the additional driving force resulting from relative motion in the transverse direction contributes to the total torsional force, thereby leading to significant rotary responses. Furthermore, the streamlined profile accounts for the escalation in vibration amplitudes.

I. INTRODUCTION

The study of flow past a circular cylinder is a fundamental problem in fluid dynamics, providing crucial insights into boundary layer separations, vortex dynamics, and wake characteristics. These phenomena are highly relevant to various natural occurrences and engineering applications, such as offshore risers and heat exchangers. Vortex shedding from the circular cylinder induces periodic pressure fluctuations, resulting in lift forces that act as significant sources of flow-induced vibrations. One of the most widely recognized and effective passive control methods involves the use of rigid splitter plates placed in the wake of a circular cylinder, initially investigated by Roshko¹ in 1954. This device induces notable changes in both wake characteristics and fluid forces acting on the cylinder, as evidenced by a lot of studies.²⁻⁵ Furthermore, research by Nakamura⁶ and Zhu *et al.*⁷ has suggested that splitter plates can delay the interaction between shear layers from the circular cylinder, leading to more stable near-wake flows and consequently reducing fluid forces.

In numerous real-world scenarios, inflow directions, such as ocean currents and atmospheric winds, often vary over time. Therefore, a rotatable splitter plate, allowing the system to accommodate different flow directions, proves to be a better choice than a fixed one. The freely-rotating and elastically mounted cylinder-plate bodies represent two fundamental scenarios. Xu *et al.*⁸ were the first to investigate laminar flow past a circular cylinder equipped with a freely-rotating splitter plate. They reported a symmetry-breaking bifurcation phenomenon⁹ wherein the cylinder-plate system shifted to an asymmetric equilibrium position. Later, Xu *et al.*¹⁰ further elucidated that the uneven flows within the separation bubble on the plate's upper and lower surfaces are the primary factors contributing to the asymmetric pressures and subsequent bifurcation phenomenon. The length of the plate plays a crucial role in determining the occurrence

of bifurcation. Both experimental results¹¹⁻¹⁴ and numerical findings¹⁵ have demonstrated that a longer plate leads to smaller deflections, reducing the likelihood of observing bifurcation when attached to the circular cylinder. Additionally, the Reynolds number significantly influences the rotation dynamics of a rotatable cylinder-plate. For instance, at a low Reynolds number of 50, bifurcation disappears when the plate length exceeds 1.7 times the cylinder diameter.⁸ However, the critical plate length associated with the disappearance of bifurcation shifts to a larger value of approximately 4 times the cylinder diameter when considering Reynolds numbers ranging between 5×10^3 and 5×10^4 .^{11, 12, 14} Considering rotational stiffness and damping, Lu *et al.*¹⁶ investigated the rotation responses of an elastically mounted cylinder-plate at $Re = 100$. Their findings indicated that for a longer splitter plate, the critical reduced velocity required for the symmetry-breaking bifurcation to occur is lower. Moreover, the rotation amplitudes of an elastically mounted cylinder-plate are substantially greater than those observed in a freely-rotating case. Zhang *et al.*¹⁷ identified that the symmetry-breaking bifurcation results from a combined effect of the structural restoring moment and the flow-induced moment.

In nature, phenomena involving flow-induced vibration in the transverse direction and flow-induced rotation in the torsional direction often coexist, as seen in the fluttering motion of leaves. Therefore, investigating the coupled responses of flow-induced vibration and rotation of a cylinder-plate holds significant importance. However, literature on this topic is relatively scarce, with most studies focusing on the effect of rotational oscillations on flow-induced vibration responses. Previous findings suggest that after accounting for rotational oscillations, the flow-induced vibrations of a cylinder-plate can either be enhanced or suppressed.¹⁸⁻²⁰ For instance, Assi *et al.*¹⁸ conducted a study comparing the significant impact of torsional friction on vibration responses. They found that enhanced vibration responses occur at a low torsional friction of $\tau_f = 0.009 \text{ Nm/m}$. Conversely, when relatively large torsional friction of $\tau_f = 0.035 \text{ Nm/m}$ is considered, the transverse vibration amplitudes of the rotatable cylinder-plate are significantly reduced. In our previous work,²⁰ we also demonstrated that for a specific cylinder-plate, passive rotations can substantially alter not only the flow-induced vibration response modes but also the vibration amplitudes. We observed a mode transformation from a full interaction between VIV and galloping to a typical VIV mode. Additionally, vibration amplitudes are reduced at low rotational reduced velocities but amplified at high rotational reduced velocities

Based on the literature reviews and analyses presented above, it is evident that there is a gap in the research concerning the effect of vibrations on the flow-induced rotation responses of a cylinder-plate. Therefore, several open questions need to be addressed: Can the vibration reduce rotation responses or not? What are the differences in movement postures between the rotation-only case and those cases considering both vibrations and rotations? Is there a relationship between response modes and wake patterns? What is the flow mechanism underlying the interaction between rotation and vibration? To this end, this work conducts numerical simulations to investigate the role of cross-flow vibrations in flow-induced rotation responses of an elastically mounted cylinder-plate. The rotation-only case with a wide rotational reduced velocity U_θ range of 2–18 is set as a benchmark case. Then four different simulation groups, spanning $U_\theta = 2$ –18 under four vibrational reduced velocities $U_y = 5, 8, 12, \text{ and } 18$, are considered. Referring to our previous work,^{20, 24} the selection of these four vibrational reduced velocities not only cover the VIV-galloping band, but also can investigate the effect of vibrational damping and stiffness.

Nomenclature

D	Diameter of the circular cylinder [m]
U	Incoming flow velocity [m s^{-1}]
μ	Dynamic viscosity of fluid [Pa s]
ρ	Density of fluid [kg m^{-3}]
Re	Reynolds number, $\rho UD/\mu$ [-]
x, y	Cartesian coordinates [-]
u, v	velocity component in x - and y -directions [m s^{-1}]
p	Pressure [Pa]
t	Flow time [s]
m	Structural mass [kg]
m^*	Mass ratio [-]
y_0	Displacement in transverse direction [m]
Y	Non-dimensional displacement, y_0/D [-]
\bar{Y}	Time-averaged displacement [-]
Y_A	Amplitudes of displacement [-]
\dot{y}_0 (u_y)	Translational velocity in transverse direction [m s^{-1}]
\ddot{y}_0 (a)	Translational acceleration in transverse direction [m s^{-2}]
K_y	Vibrational stiffness constant [kg s^{-2}]
C_y	Vibrational damping constant [kg s^{-1}]

ζ_y	Vibrational damping ratio, $C_y/(2\sqrt{K_y m})$ [-]
F_L	Lift force [N]
C_L	Lift coefficient, $2F_L/(\rho U^2 D)$ [-]
U_y	Vibrational reduced velocity, $U/(f_{ny} D)$ [-]
f_{ny}	Vibrational natural frequency, $1/(2\pi)\sqrt{K_y/m}$ [s ⁻¹]
f_y^*	Vibrational frequency ratio, normalized by f_{ny} [-]
θ	Rotary angle [radian]
$\bar{\theta}$	Time-averaged rotary angle [radian]
θ_A	Amplitudes of rotary angle [radian]
$\dot{\theta}$	Rotary velocity [radian s ⁻¹]
$\ddot{\theta}$	Rotary acceleration [radian s ⁻²]
I_θ	Mass moment of inertia [kg m ²]
I_θ^*	Normalized mass moment of inertia, $I_\theta/(\rho D^4)$ [-]
K_θ	Rotational stiffness constant [kg s ⁻²]
C_θ	Rotational damping constant [kg s ⁻¹]
ζ_θ	Rotational damping ratio, $C_\theta/(2\sqrt{K_\theta I_\theta})$ [-]
M_θ	Moment with respect to the cylinder center [N m]
C_M	Pitching moment coefficient, $2M_\theta/(\rho D^2 U^2)$ [-]
U_θ	Rotational reduced velocity, $U/(f_{n\theta} D)$ [-]
$f_{n\theta}$	Rotational natural frequency, $1/(2\pi)\sqrt{K_\theta/I_\theta}$ [s ⁻¹]
f_θ^*	Rotational frequency ratio, normalized by $f_{n\theta}$ [-]
$\varphi_{\theta-y}$	Phase angle between displacement and rotary angle [°]
U^*	Resultant velocity, composed of U and $-u_y$ [m s ⁻¹]

II. PROBLEM DESCRIPTION AND METHODOLOGY

As illustrated in Fig. 1, a rigid splitter plate is affixed to the rear of a circular cylinder, where the cylinder diameter, plate length, and plate width are D , D , and $0.1D$, respectively. The whole cylinder-plate system is elastically mounted in both transverse and torsional directions. When the fluid-structure interaction occurs, the cylinder-plate triggers transverse vibration and torsional rotation responses and moves to a new position (y_0, θ) , where the transitional displacement y_0 and

rotary angle θ are positive when the cylinder-plate oscillates in upward and counterclockwise directions, respectively.

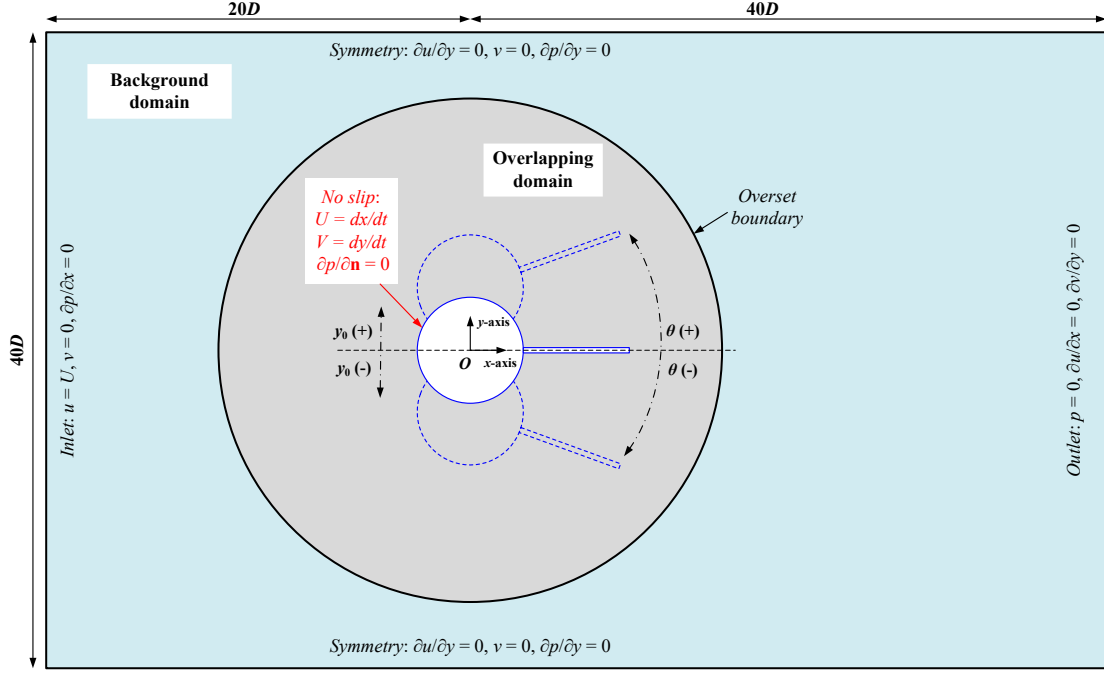


FIG. 1. Sketch of flow over an elastically mounted cylinder-plate system.

In this work, the dynamics of the cylinder-plate is numerically investigated at a low Reynolds number of $Re = 120$. Therefore, the two-dimensional laminar flow field can be described by the incompressible Navier-Stokes equations including the continuity and momentum equations.²¹

$$\frac{\partial u}{\partial x} + \frac{\partial v}{\partial y} = 0 \quad (1)$$

$$\rho \left(\frac{\partial u}{\partial t} + u \frac{\partial u}{\partial x} + v \frac{\partial u}{\partial y} \right) = -\frac{\partial p}{\partial x} + \mu \left(\frac{\partial^2 u}{\partial x^2} + \frac{\partial^2 u}{\partial y^2} \right) \quad (2)$$

$$\rho \left(\frac{\partial v}{\partial t} + u \frac{\partial v}{\partial x} + v \frac{\partial v}{\partial y} \right) = -\frac{\partial p}{\partial y} + \mu \left(\frac{\partial^2 v}{\partial x^2} + \frac{\partial^2 v}{\partial y^2} \right) \quad (3)$$

where x and y are the coordinates in the inline and cross-flow direction, respectively; u and v the velocity component in the x - and y -directions, respectively; ρ the fluid density; p the pressure; t the time; and μ the dynamic viscosity.

According to Newton's second law of motion, the equations governing flow-induced vibration and rotation of the present system can be expressed by equations (4) and (5), respectively. Equations (6) and (7) show the associated non-dimensional formats, respectively. Definition of

symbols in equations (4)–(7) can be found in nomenclature and key parameters in this work are set as: $m^* = 6.9$, $\zeta_y = 0.01$, $I_\theta^* = 1.426$, $\zeta_\theta = 0.001$.

$$m\ddot{y}_0 + C_y\dot{y}_0 + K_y y_0 = F_L \quad (4)$$

$$I_\theta\ddot{\theta} + C_\theta\dot{\theta} + K_\theta\theta = M_\theta \quad (5)$$

$$\ddot{Y} + 2\zeta_y\left(\frac{2\pi}{U_y}\right)\dot{Y} + \left(\frac{2\pi}{U_y}\right)^2 Y = \frac{C_L}{2m^*} \quad (6)$$

$$\ddot{\theta} + 2\zeta_\theta\left(\frac{2\pi}{U_\theta}\right)\dot{\theta} + \left(\frac{2\pi}{U_\theta}\right)^2 \theta = \frac{C_M}{2I^*} \quad (7)$$

To solve the fluid-structure interaction, ANSYS-FLUENT package was employed with the help of in-house developed user-defined function (UDF). The finite volume method (FVM) and the coupled scheme was adopted for the pressure-velocity coupling. As shown in Fig.2, in each time-step, the flow field is first obtained by solving equations (1)–(3). After that, the hydrodynamic forces are calculated by conducting an integration involving the pressure and viscous stress. Finally, the displacement and rotary angle are computed by substituting the hydrodynamic forces into equations (4) and (5), which are discretized by an improved fourth-order Runge-Kutta method.²² Accordingly, the cylinder-plate moves to a new position and the computational mesh is updated for the calculation of flow field at the next time step. For reliable statistical analysis, the residual of 10^{-5} was selected as the convergent criteria for the iterations, and the calculation was running until sufficient periodic results (more than 50 cycles) were obtained.

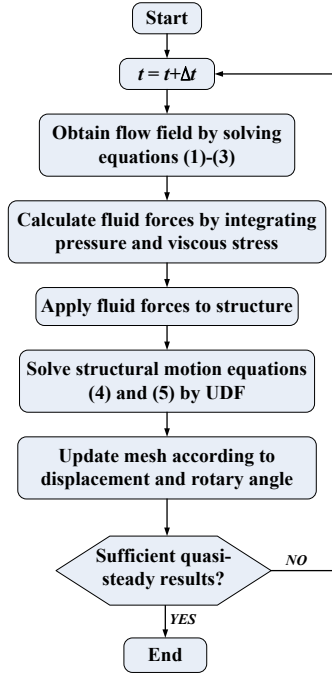


FIG. 2. Numerical calculation procedure.

In this study, the overlapping mesh method is employed to address both the vibration and rotation motions. The computational domain and boundary conditions are described in Fig. 1. In the current two-dimensional simulations, a rectangular background domain of $60D$ length and $40D$ width is utilized. The distances from the cylinder center to the upstream boundary and two bilateral boundaries are all $20D$. A concentric circle containing the cylinder-plate is specified as the overlapping domain, and its diameter is $20D$ according to the independence study result.²⁰ Regarding the boundary conditions, a steady uniform velocity is applied at the inlet. The pressure-outlet condition is set at the downstream boundary to ensure a fully developed flow. At two lateral boundaries, the normal component of the velocity and the tangential component of the wall shear stress are set to zero. A no-slip condition is specified at the surface of the cylinder-plate. Given that the physical model in this work is identical to that used in our previous research,²⁰ details regarding the CFD mesh, grid and time-step independence study, and numerical method validation are not reiterated here.

III. RESULTS AND DISCUSSION

A. Bifurcation phenomenon

According to Crawford and Knobloch,⁹ when an equilibrium system undergoes a symmetry-breaking bifurcation, new fluid states appear that have less symmetry and frequently

more complicated dynamics. The loss of symmetry is manifested by the appearance of a new pattern. In this work, symmetry-breaking bifurcation refers to a phenomenon wherein the symmetric cylinder-plate body transitions to an asymmetric equilibrium position, resulting in non-zero time-averaged displacements or rotary angles. Figure 3 illustrates typical results of both non-bifurcation and bifurcation cases, showcasing the time histories of displacement and rotary angle, as well as the trajectories of vibration velocity versus displacement, and rotary velocity versus rotary angle

As depicted in Fig. 3(a), both the rotary angle and displacement exhibit an initial increase with time, followed by noticeable flapping motions observed around $t^* \approx 80$, and subsequently transitioning into well-organized and harmonic responses. Furthermore, during the quasi-steady stage of $t^* = 200\text{--}280$, both the time-averaged rotary angle and displacement are zero, indicating the absence of bifurcation phenomenon. As noted by Lu *et al.*¹⁶ and Tang *et al.*²³, the spiral patterns in terms of $\dot{\theta}$ v.s. θ and \dot{Y} v.s. Y not only illustrate the rotating and vibrating process but also signify the presence of bifurcation, offering valuable insights into fluid-structure interactions. As shown in Figs. 3(c) and 3(e), the Lissajous figures display a convergent solution with a single clear limit cycle, as highlighted by the red dashed lines. These steady cycle trajectories are consistently symmetrical about $Y = 0$ and $\theta = 0$, indicating non-bifurcation responses. However, upon increasing the reduced velocity to $U_\theta = 14$, the rotation and vibration developments markedly differ from those at $U_\theta = 5$. The rotary angle and displacement signals depicted in Fig. 3(b) undergo three stages: an unstable flapping stage, a deflection from zero to negative values, and a stable stage with regular flapping motions. Notably, the deflection processes confirm the existence of symmetry-breaking bifurcation. As shown in Figs. 3(d) and 3(f), the Lissajous figures in bifurcation region reveal two loops and a transition stage, which correspond to the three stages observed in Fig. 3(b). The unstable stage, highlighted by blue dashed lines, originates from the initial conditions of $Y = 0$ and $\theta = 0$, while the stable solution develops from the former loop after the deflection.

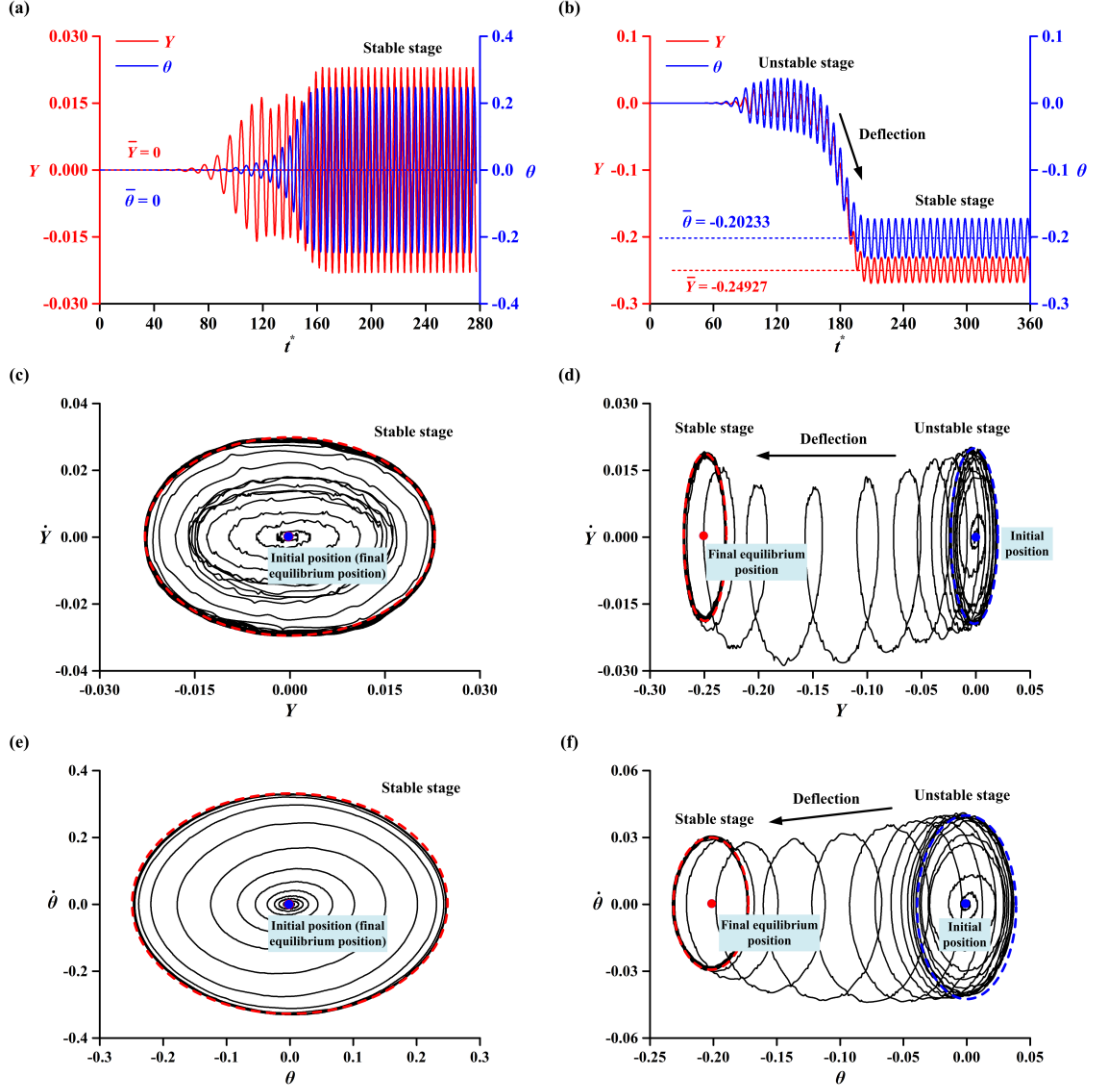


FIG. 3. Non-bifurcation (left column) and bifurcation (right column) signals: (a) and (b) are time histories of displacement and rotary angle; (c) and (d) show the trajectory of vibration velocity v.s. displacement; (e) and (f) show the trajectory of rotary velocity v.s. rotary angle. Blue and red points represent the initial position and final equilibrium position, respectively.

Figure 4 provides an overview of non-bifurcation and bifurcation phenomena to explore the effects of U_θ and U_y , including the rotation-only case for comparisons. For relatively low vibrational reduced velocities of $U_y = 5$ and $U_y = 8$ in Figs. 4(a) and 4(c), horizontal lines of $\bar{Y} = 0$ and $\bar{\theta} = 0$ are evident across the entire U_θ range of 2–18, indicating the non-bifurcation responses. However, an increase in the vibrational reduced velocity leads to the occurrence of bifurcation phenomenon. As displayed in Fig. 4(b) and 4(d), the time-averaged rotary angle and displacement remain zero in the range of $U_\theta = 2$ –12, while distinct net deflections to either

positive or negative values are clearly observed in the rest range, confirming the appearance of bifurcation. Within the bifurcation region, both \bar{Y} and $\bar{\theta}$ are dependent on U_θ and U_y . Figure 4(b) shows that \bar{Y} at $U_y = 18$ firstly experiences a sharp increase in the range of $U_\theta = 12-14$, then following by a slight decrease. In contrast, \bar{Y} at $U_y = 12$ show a smoothly increasing trend. As depicted in Fig. 4(d), the variations of $\bar{\theta}$ at $U_y = 18$ closely follow the trend of rotation-only case, This can be attributed to the smaller vibrational damping and stiffness at higher U_y , consequently resulting in less impact on rotation responses.

To further understand the appearance of symmetry-breaking bifurcation, the associated physical reason can be provided with the help of assumptions by Xu *et al.*¹⁰. There is a region of separated flow behind a bare circular cylinder where there are two stationary or alternatively shedding vortices. Now consider a splitter plate of such small plate length that it does not affect the flow pattern. If free to rotate, the $\theta = 0$ position of this cylinder-plate system will not be stable, since the flow near the splitter plate is towards the cylinder. The cylinder-plate system will rotate and the splitter plate will migrate to an angle near the point at the surface of the cylinder where separation begins. Experimentally, this angle was found to be nearly 80° for a very small plate length of $0.06D$, the splitter plate used by Cimbala and Garg.¹² With increasing the plate length, the offsetting angle will decrease and finally become to be zero. For a $1D$ splitter plate, the offsetting angle is about 20 degrees when the cylinder-plate system can rotate freely.¹¹⁻¹⁴

In this work, both the vibrational and rotational damping and stiffness are considered, which present distinct dynamic behaviors as compared with the freely-rotating case. As depicted in Fig. 4, the symmetry-breaking bifurcation is not observed in the entire U_θ range at $U_y = 5$ and $U_y = 8$ as well as the range of $U_\theta = 2-12$ at $U_y = 12$ and $U_y = 18$. However, when both U_θ and U_y are relatively large, symmetry-breaking bifurcation appears, indicating the less influence of damping and stiffness. This finding also shows that cylinder-plate system at larger reduced velocities is much similar to the freely-rotating case.

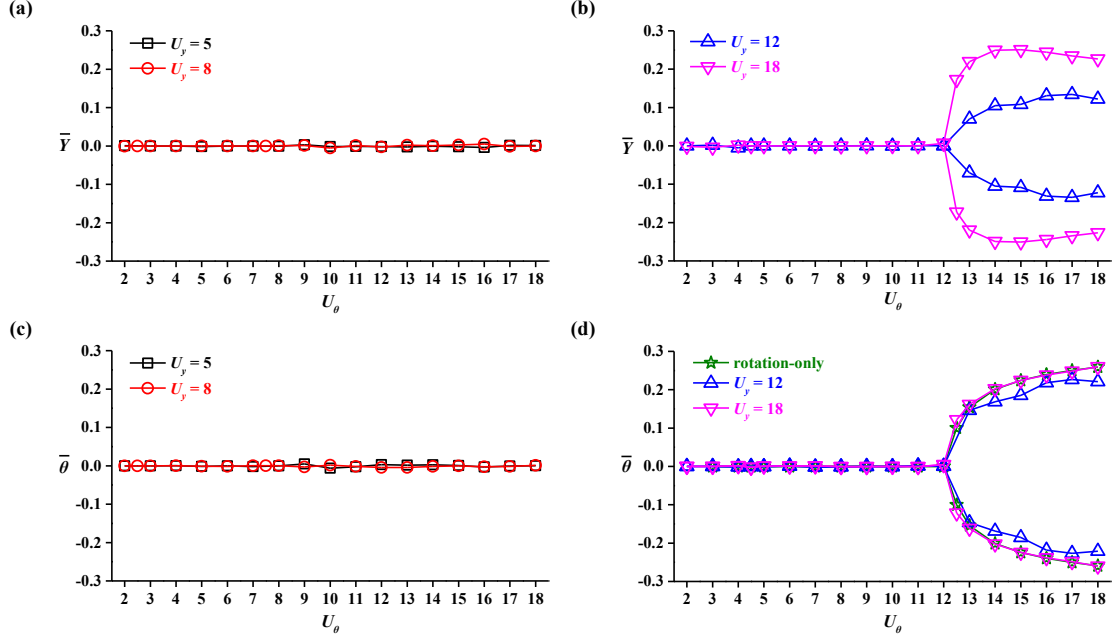


FIG. 4. An overview of the non-bifurcation (left column) and bifurcation (right column) phenomena: (a) and (b) show the time-averaged displacements; (c) and (d) show the time-averaged rotary angles.

B. Response modes

Based on the variations of vibration and rotation amplitudes and frequencies depicted in Figs. 6 and 7, four distinct response modes are identified, as shown in Fig. 5. The line of $St = 0.145$ in the frequency variations present the non-dimensional vortex shedding frequency of the stationary cylinder-plate system, which has been obtained in our previous work.²³ These four response modes are categorized as follows: vibration-dominated mode, rotation-dominated mode, augmentation with a VIV-like mode, and augmentation with a galloping-like mode. The vibration-dominated mode refers to such a configuration in which the vibration amplitudes of the cylinder-plate considering both vibration and rotation closely resemble those of vibration-only case, while the rotation amplitudes remain nearly zero. This mode is primarily observed at relatively low rotational reduced velocities, as indicated by the white circles in Fig. 5, and it can be attributed to the larger rotational damping and stiffness, which resist rotations despite the relatively large vibration amplitudes in some cases. In contrast, the second response mode (rotation-dominated mode) signifies that the rotation amplitudes of current case closely match those of rotation-only case, while the vibration amplitudes are nearly zero. This mode is observed in the range of $U_\theta = 2.5-7$ at $U_y = 8$, $U_\theta = 4.5-11$ at $U_y = 12$, and $U_\theta = 4.5-18$ at $U_y = 18$, as shown

in Fig. 5. It is evident that the a wider U_θ range for the rotation-dominated mode is achieved at larger U_y , primarily due to the smaller vibrational damping and stiffness, resulting in reduced vibrational influence.

In other cases, both the vibration and rotation responses are significantly enhanced, and two augmentation modes (VIV-like and galloping-like) are identified. The VIV-like mode appears within the range of $U_\theta = 5\text{--}18$ at $U_y = 5$, as depicted in Fig. 5. The amplitudes of this mode in Fig. 6(a) and Fig. 7(a) are larger than those of vibration-only/rotation-only cases, although exhibiting a decreasing trend with increasing U_θ . Besides, the dimensionless frequencies closely adhere a Strouhal law, further confirming the VIV response. Referring to Fig. 5, the galloping-like mode is observed in the range of $U_\theta = 7.5\text{--}18$ at $U_y = 8$ and $U_\theta = 12\text{--}18$ at $U_y = 12$. The vibration and rotation amplitudes in Figs. 6(b), 6(c), 7(b), and 7(c) rise sharply at the onset reduced velocity of $U_\theta = 7.5$ and $U_\theta = 12$, respectively, followed by continuous growth. Consequently, the amplitudes exceed those of vibration-only/rotation-only case. Additionally, the frequencies deviate from the Strouhal law, exhibiting lower values that confirm the presence of galloping responses.

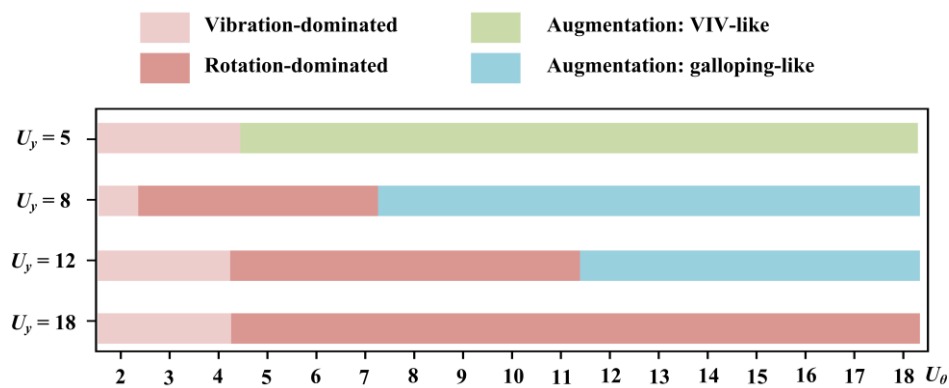


FIG. 5. An overview of response modes.

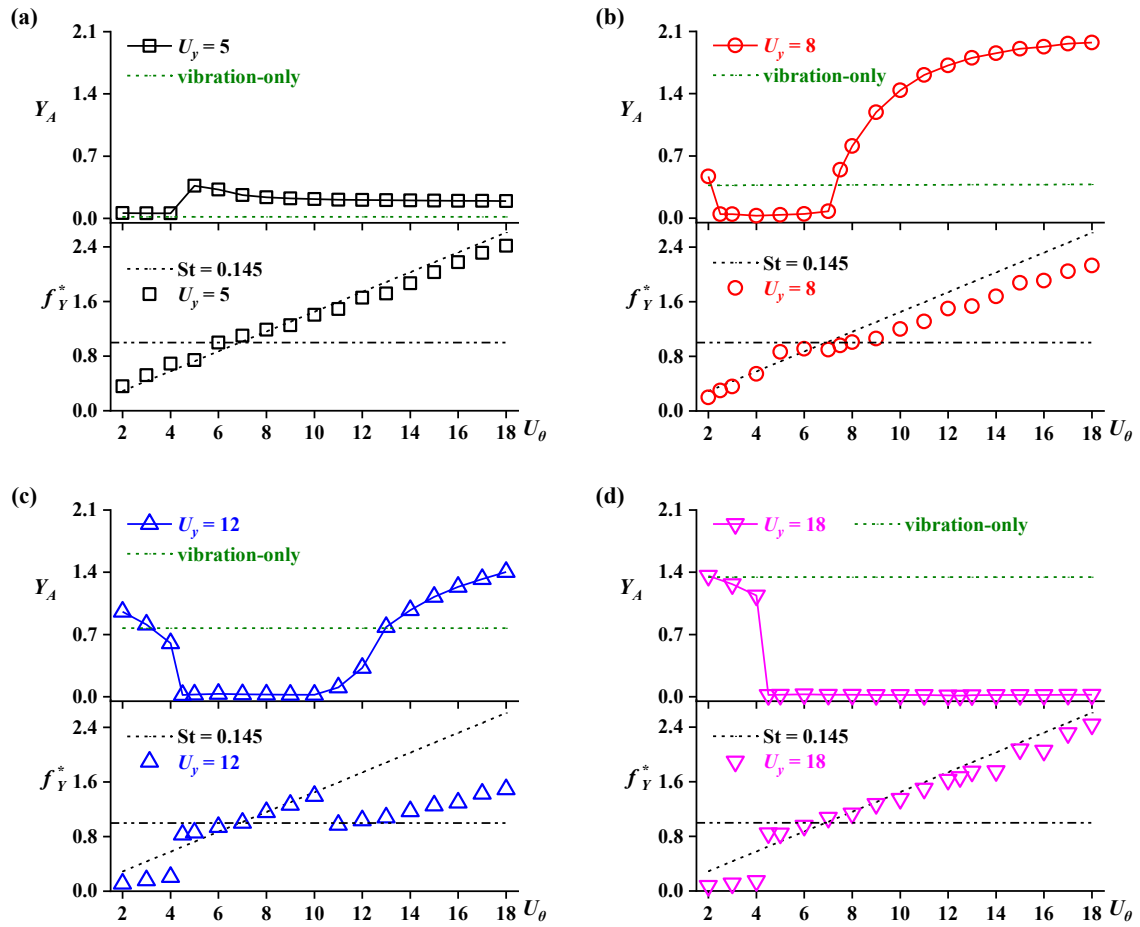


FIG. 6. Vibration amplitude and frequency responses: (a) $U_y = 5$, (b) $U_y = 8$, (c) $U_y = 12$, and (d) $U_y = 18$.

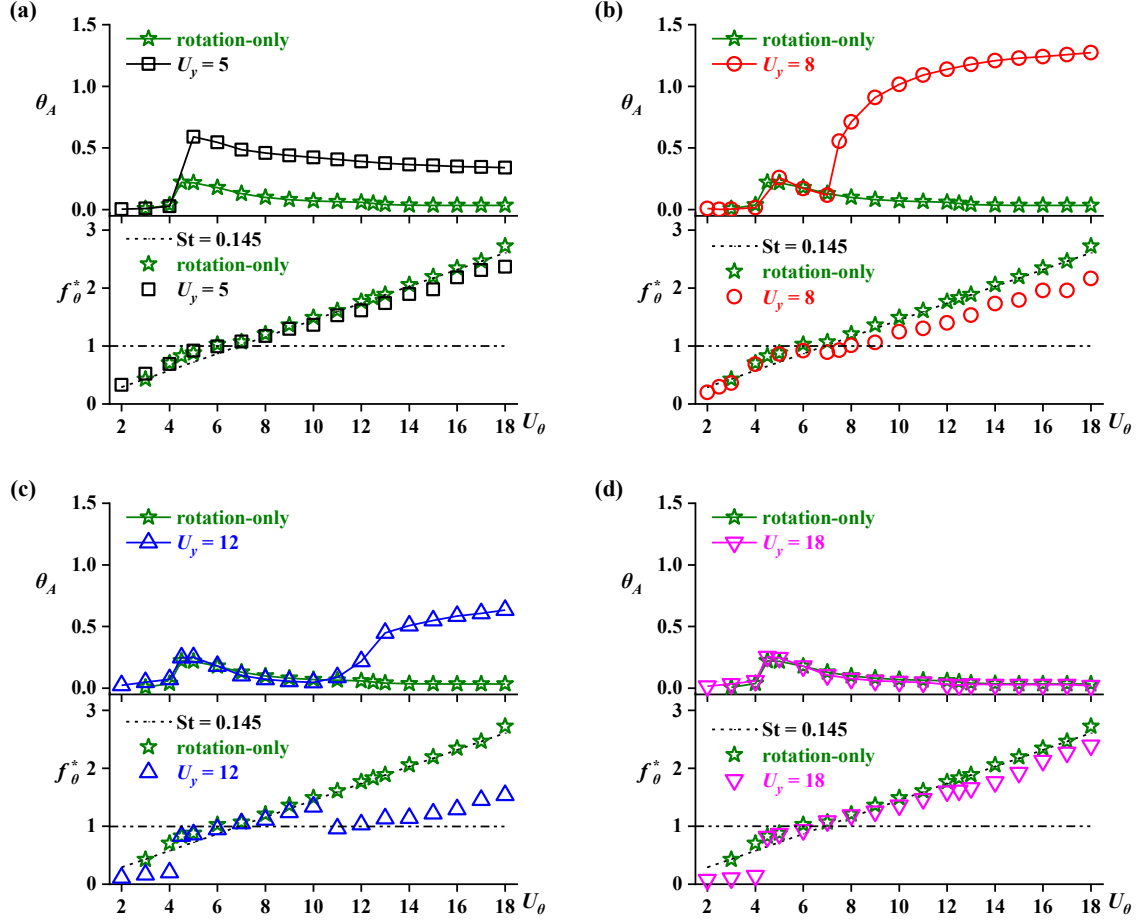


FIG. 7. Rotation amplitude and frequency responses: (a) $U_y = 5$, (b) $U_y = 8$, (c) $U_y = 12$, and (d) $U_y = 18$.

Figure 8 compares the phase angles $\varphi_{\theta-Y}$ at four different vibrational reduced velocities. At $U_y = 5$, phase angles vary smoothly with increasing U_0 : starting from $\varphi_{\theta-Y} \approx 60^\circ$, then gradually rising, and finally remaining at a steady horizontal line of $\varphi_{\theta-Y} \approx 180^\circ$. This procession reflects a shift of response modes from vibration-dominated mode to VIV-like mode, as depicted in Fig. 5. In contrast, variations of $\varphi_{\theta-Y}$ at $U_y = 8$, $U_y = 12$, and $U_y = 18$ are relatively complex. Specifically, two sharp rises are observed at $U_y = 8$ and $U_y = 12$, as shown in Figs. 8(b) and 8(c): the first one occurs at low rotational reduced velocities, corresponding to the switch from vibration-dominated mode to rotation-dominated mode, and the second rise is observed when the response mode changes from rotation-dominated mode to galloping-like mode. In Figs. 8(d), only one sharp rise from vibration-dominated mode to rotation-dominated mode is observed. Generally, phase angles in rotation-dominated region show a continuous decreasing trend while remain nearly 90° in galloping-like region. Besides, it can be concluded that the switch between rotation and vibration

responses leads to the sharp rise in phase angle of displacement versus rotary angle.

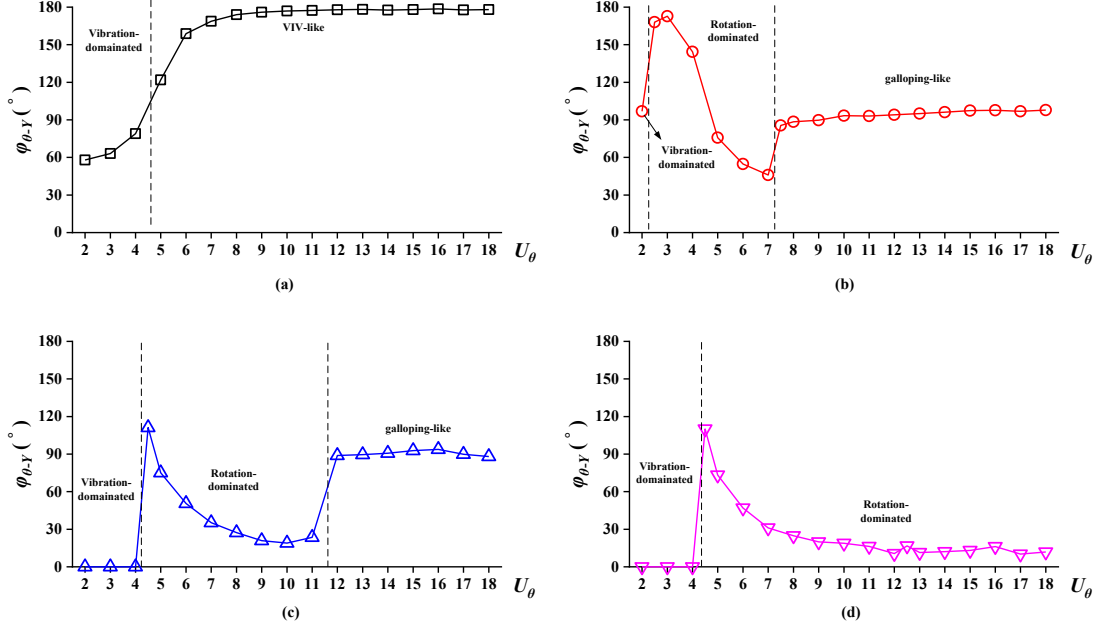


FIG. 8. Phase angles of displacement versus rotary angle: (a) $U_y = 5$, (b) $U_y = 8$, (c) $U_y = 12$, and (d) $U_y = 18$.

Phase angles of displacement versus rotary angle can be used to reflect the movement posture of the cylinder-plate. Figure 9 illustrates four typical motion types to elucidate the relationship between vibration and rotation responses. As shown in Fig. 9(a), the cylinder-plate primarily maintains a horizontal posture, exhibiting relatively large amplitudes in transverse direction while undergoing minor adjustments in the torsional direction, indicative of the vibration-dominated mode. In contrast, the cylinder-plate in rotation-dominated region appears relatively static, as depicted in Fig. 9(b). For galloping-like mode in Fig. 9(c), the instantaneous structural postures consistently maintain a streamlined configuration, with the phase angle of $\varphi_{\theta-\gamma} \approx 90^\circ$. Here, “streamlined” refers to a configuration wherein the splitter plate remains positioned rearward of the circular cylinder concerning the resultant velocity. The resultant velocity is defined as a vector composed of incoming flow velocity and vibrational velocity. At positions corresponding to the maximum or minimum displacement, the vibrational velocity is zero, causing the resultant velocity to align nearly horizontally. Simultaneously, the cylinder-plate maintains a predominantly horizontal orientation, resulting in a streamlined profile. As the body moves between its maximum positive and negative positions, the splitter plate remains concealed behind the circular cylinder, further contributing to the streamlined profile. This dynamic response illustrates the

cylinder-plate's ability to adjust its posture, aiming for drag reduction and consequently augmenting both vibration and rotation. The coupled movements at $\varphi_{\theta-Y} \approx 180^\circ$ are displayed in Fig. 9(d). Observations reveal a notable difference in the projected area between the VIV-like region in Fig. 9(d) and galloping-like region in Fig. 9(c), particularly in the transverse direction. This disparity suggests a higher allocation of energy towards inducing rotation of the splitter plate when the cylinder-plate undergoes vibration, consequently leading to relatively reduced vibration and rotation amplitudes in the VIV-like mode.

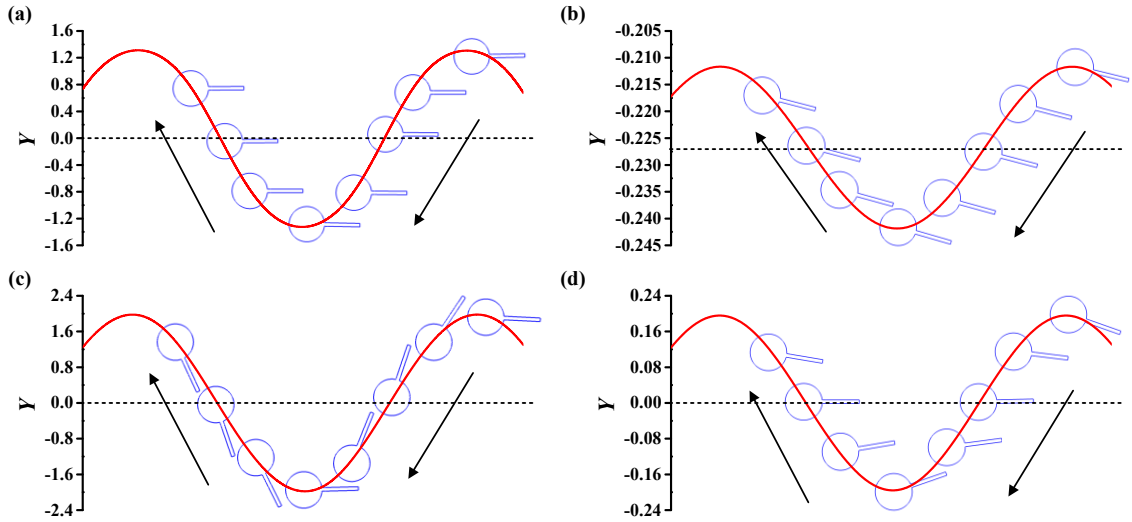


FIG. 9. Typical motion types: (a) $\varphi_{\theta-Y} \approx 0^\circ$ at $U_\theta = 2$ and $U_y = 18$ in vibration-dominated region; (b) $\varphi_{\theta-Y} \approx 0^\circ$ at $U_\theta = 18$ and $U_y = 18$ in rotation-dominated region; (c) $\varphi_{\theta-Y} \approx 90^\circ$ at $U_\theta = 18$ and $U_y = 8$ in galloping-like region; and (d) $\varphi_{\theta-Y} \approx 180^\circ$ at $U_\theta = 18$ and $U_y = 5$ in VIV-like region, where the black arrow represents the vibration direction.

C. Vortex shedding modes

In our previous investigation²⁰ where $U_y = 3-18$ under $U_\theta = 5, 8, 12,$ and 18 were studied, four different vortex shedding modes including 2S (two single vortices), 2P (two pairs of vortices), 2S*, and 2T (two triplets of vortices) were identified, where the 2S* mode consists of two single vortices, each exhibiting a tendency to split into two smaller vortices as they migrate downwards. In this work, a range of $U_\theta = 2-18$ under $U_y = 5, 8, 12,$ and 18 are considered, and more vortex shedding modes are observed. Figure 10 summarizes the vortex shedding modes, responses modes, and bifurcation region of the present cylinder-plate. For the rotation-only case, 2S mode appears across the entire U_θ range, regardless of the presence of bifurcation or non-bifurcation region. The difference observed in 2S mode between the bifurcation and non-bifurcation region will be

detailed and discussed in Fig. 11. Similarly at $U_y = 5$, the 2S mode spans the entire U_θ range, which can be attributed to the relatively small vibration and rotation amplitudes in the vibration-dominated mode and VIV-like region. As the vibrational reduced velocity increases, more complex vortex shedding modes emerge. At $U_y = 8, 12,$ and 18 , the 2T mode dominates the vibration-dominated region due to the large vibration amplitudes. However, as the cylinder-plate enters the the rotation-dominated region, the vibration amplitudes diminish, resulting in the prevalence of the 2S mode. In the galloping-like region where amplitudes increase continuously with U_θ , the wake modes successively transition from 2S to $2S^*$ and then to 2P mode for $U_y = 8$. For $U_y = 12$, the wake modes transition from 2P to P+S (one pair and one single vortices), and finally to 2P+S (two pairs and one single vortices). Referring to our previous study²⁴, only 2S and 2P mode were observed for the vibration-only case under the same simulation conditions. In contrast, the current study reveals seven distinctly different wake modes, indicating significant interactions between rotation and vibration responses. To further elucidate these vortex shedding modes, Figs. 11–15 depict typical evolutions over one vibration period. Eight instantaneous instants, starting from the maximum vibration displacement curve, are plotted to capture key movements and vorticity fields. The yellow solid lines in vorticity snapshots represent the contour of $u = 0$, facilitating the identification of the recirculation region.

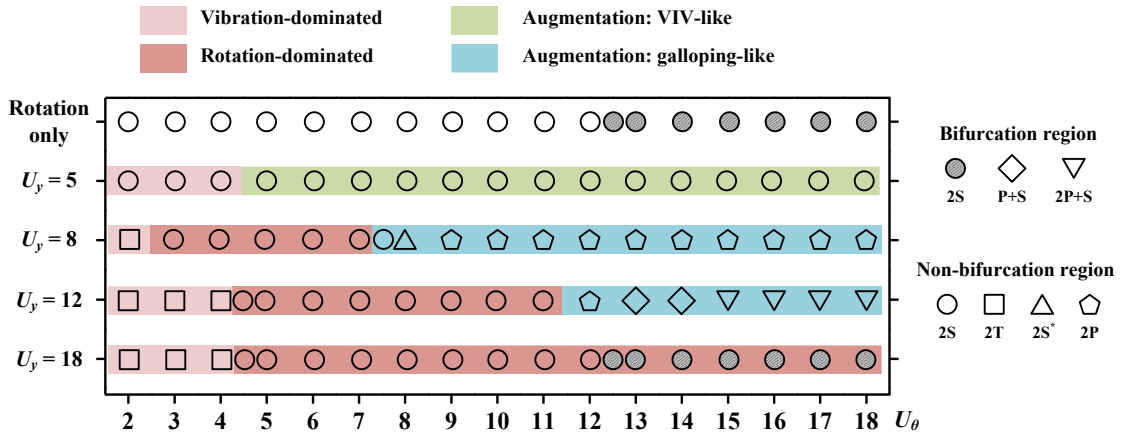


FIG. 10. Overview of vortex shedding modes for the present cylinder-plate system.

(1) 2S and $2S^*$ mode

Figure 15 compares the 2S mode in non-bifurcation and bifurcation region. In contrast to the 2S mode observed in the vibration-only case²⁴ where the shear layers directly skim over the cylinder-plate, reattachment behaviors occur more easily for the cylinder-plate considering both

vibration and rotation responses. This phenomenon is primarily attributed to the rotational oscillations. As shown in Fig. 11(a), shear layers separated from the cylinder surface alternatively bypass and are cut off by the plate tip, leading to regular single vortices and hence the typical 2S mode. After the symmetry-breaking bifurcation, the wake flow and reattachment behavior exhibit notable differences compared to the case without bifurcation, despite both cases featuring the same vortex shedding mode. As seen in Fig. 11(b), the cylinder-plate rotates clockwise and settles into a new equilibrium position, causing an asymmetric configuration relative to the flow direction. Due to the relatively small vibration and rotation amplitudes, the cylinder-plate appears nearly stationary. A noteworthy observation is that in the presence of the bifurcation, the lower shear layer consistently reattaches to the plate tip, while reattachment does not occur on the upper side of the cylinder-plate. Consequently, vortices S1 and S2, characterized by different sizes, are shed from the upper surface of the cylinder and the plate tip, respectively. The contour line of $u = 0$ highlights the simplified reattachment behavior in the bifurcation region. Additionally, the recirculation region exhibits a significantly increased length compared to the non-bifurcation region.

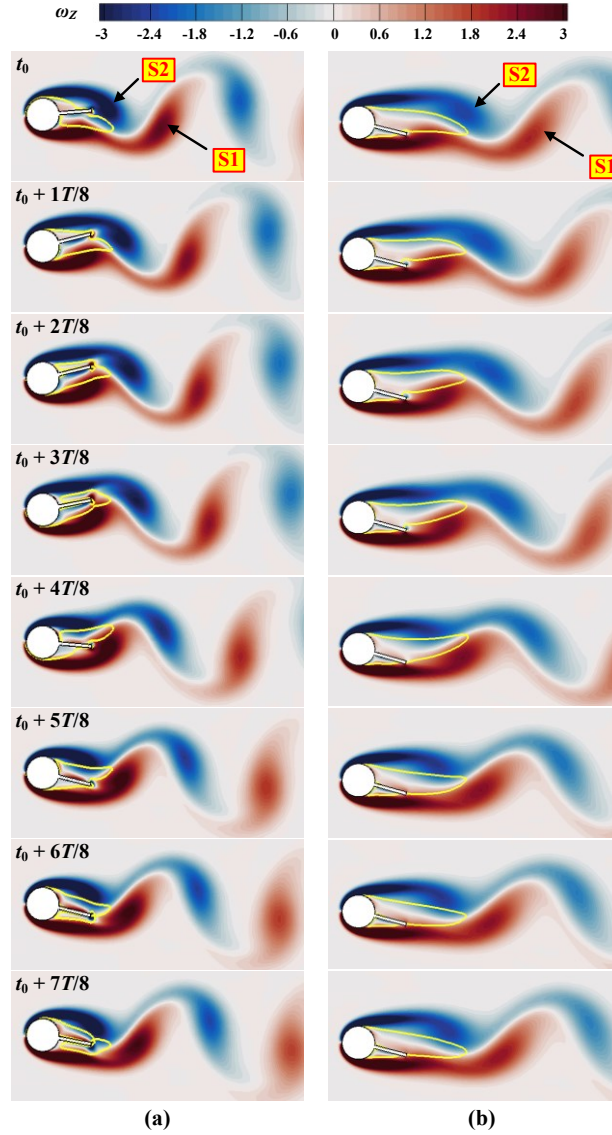


FIG. 11. Comparison of 2S mode in (a) non-bifurcation region at $U_y = 18$ and $U_\theta = 5$ and (b) bifurcation region at $U_y = 18$ and $U_\theta = 18$, where the eight continuous snapshots are picked in one vibration cycle and t_0 represents the instant corresponding to the maximum displacement.

As shown in Fig. 12, following the shedding from the cylinder-plate, the isolated vortex tends to split into two smaller vortices, leading to $2S^*$ mode. This unique vortex shedding mode can be attributed to the presence of a splitter plate and coupled responses of flow-induced vibration and rotation. The vortex splitting phenomenon was also reported by Govardhan and Williamson²⁵ for a single circular cylinder, and they believed that it is primarily due to high-amplitude oscillations. However, it should be noted that the complete splitting process is not fully realized as the vortex migrates downwards. Instead, only one core is observed in each vortex within the far wake field. This observation indicates that the $2S^*$ vortex shedding mode arises as a combined result of

high-amplitude vibrations and influence of viscous forces.

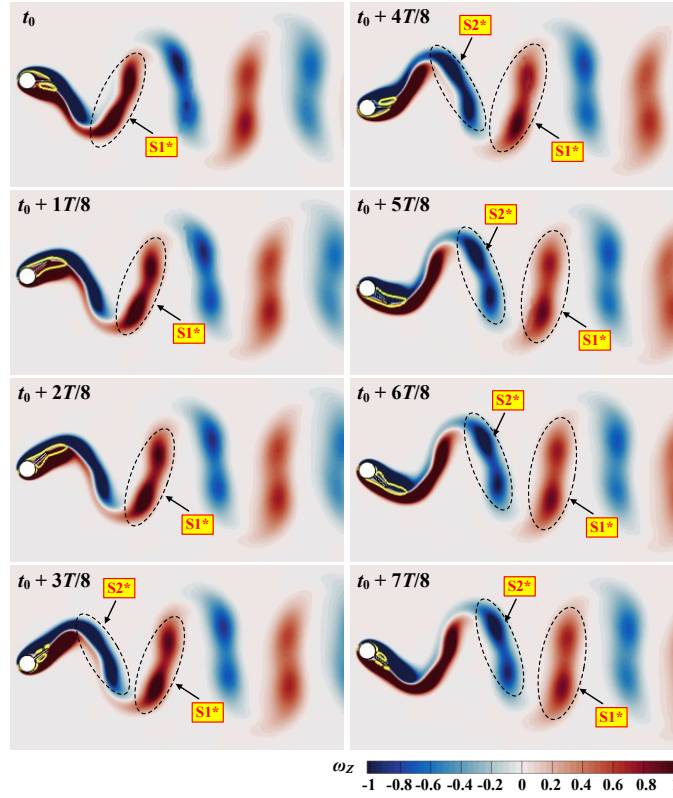


FIG. 12. Evolution of $2S^*$ mode within one vibration cycle starting from the maximum displacement ($U_y = 8$ and $U_\theta = 8$).

(2) P+S and 2P+S mode

Usually, irregular vortex shedding behaviors can be observed for bluff bodies with asymmetrical cross-sections like trapezoidal and triangular cylinder.²⁶ In this work, after the symmetry-breaking bifurcation, the cylinder-plate moves to a new equilibrium position which is not parallel to the oncoming flow direction, leading to an asymmetrical configuration and thus irregular vortex shedding modes. Referring to Fig. 10, P+S and 2P+S mode are clearly confirmed in bifurcation region. Figures 13–14 present these two wake modes within one vibration period. For P+S mode in Fig. 13, the cylinder-plate undergoes a downward motion from t_0 to $t_0+4T/8$, and a pair of vortices are shed behind the plate. In the next half period where the bluff body moves upwards, just a single vortices is observed to be shed from the lower side of the cylinder-plate, which is attributed to the negative deflection. As a result, P+S mode is identified.

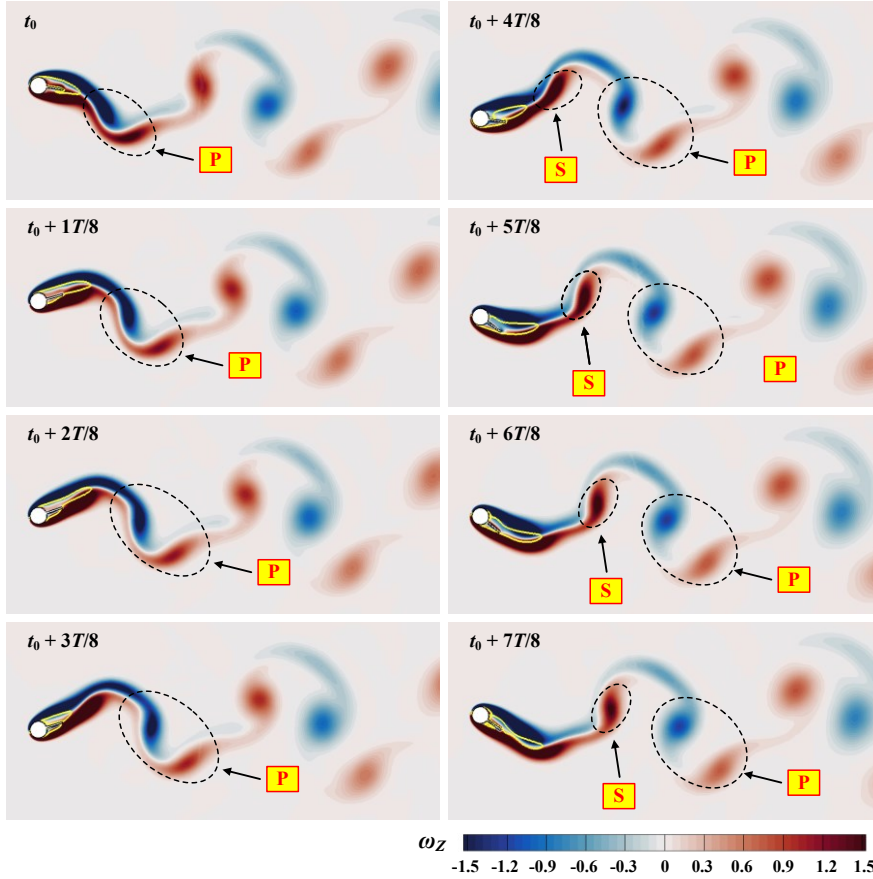


FIG. 13. Evolution of P+S mode within one vibration cycle starting from the maximum displacement ($U_y = 12$ and $U_\theta = 14$).

Large-amplitude oscillations in the transverse direction is helpful to vortex splitting²⁵ and causes more complex vortex shedding modes. For the case at $U_y = 12$ and $U_\theta = 18$ in Fig. 14, the vibration amplitude is larger than that in Fig. 13. Therefore, more vortices are shed from the cylinder-plate, and 2P+S mode is observed. Interestingly, the shedding order of these vortices is P1, S, and P2, and the single vortex S is situated in the middle between P1 and P2. Besides, it can be clearly found that the two vortices in P1 are similar in size while totally different for those in P2, revealing the effect of bifurcation.

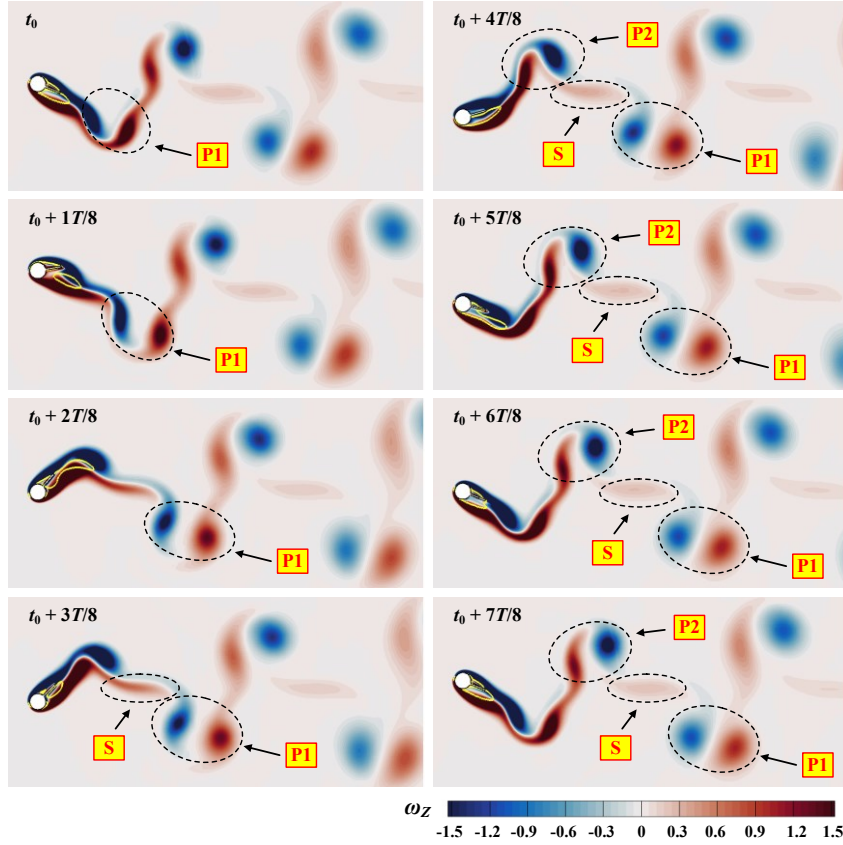


FIG. 14. Evolution of 2P+S mode within one vibration cycle starting from the maximum displacement ($U_y = 12$ and $U_\theta = 18$).

(3) 2P and 2T mode

The 2P vortex shedding mode appears in the non-bifurcation region, exhibiting a symmetric configuration. As shown in Fig. 15, two pairs of vortices are identical and shed alternately from the two sides of the cylinder-plate. Due to the large-amplitude oscillations, the vortex size in each pair of vortices shows significant differences: one appears as a circle while another one presents in a strip form. Consequently, the striped vortices dissipate so quickly and two-rowed wake mode like 2S mode is clearly observed in the far-wake filed.

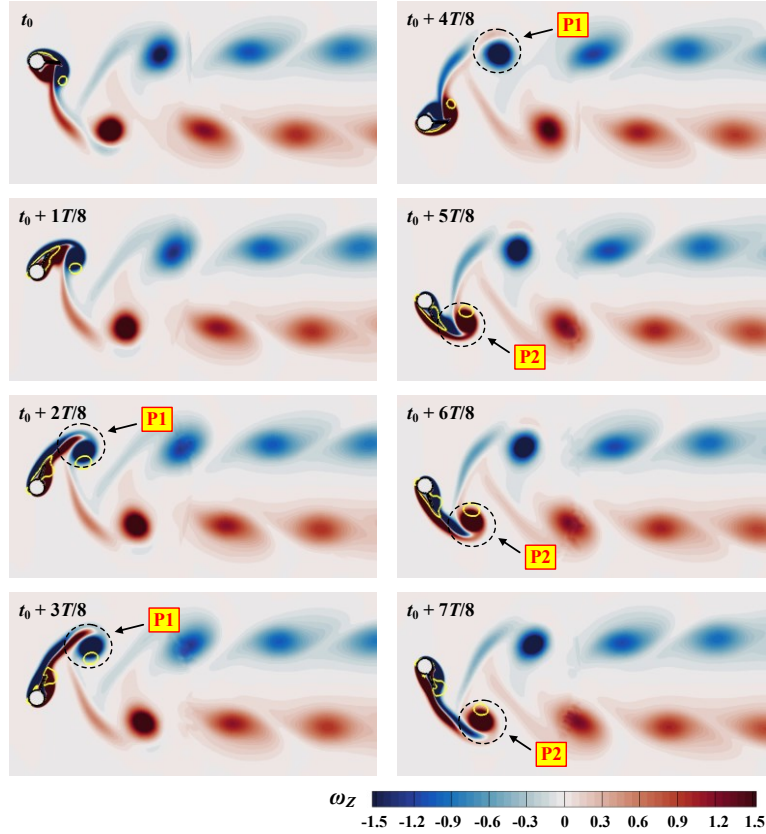


FIG. 15. Evolution of 2P mode within one vibration cycle starting from the maximum displacement ($U_y = 8$ and $U_\theta = 18$).

According to Williamson and Jauvtis²⁷, the 2T vortex shedding mode comprises two triplets of vortices in each period. As depicted in Fig. 16, T1 and T2 alternately shed behind the cylinder-plate, and those three vortices in T1/T2 possess similar size. In this work, 2T mode appears in the vibration-dominated region where vibration amplitudes are similar with those of vibration-only case while rotation amplitudes are relatively much smaller. However, it is noteworthy that the influence of rotation oscillations can not be ignored. For the vibration-only case at $U_y = 18^{24}$, galloping response was identified and associated 2P vortex shedding mode was observed. After taking into account rotation oscillations, 2T mode appears as shown in Fig. 16, indicating that the rotating splitter plate is helpful to cut off the shear layers, thereby generating more vortices.

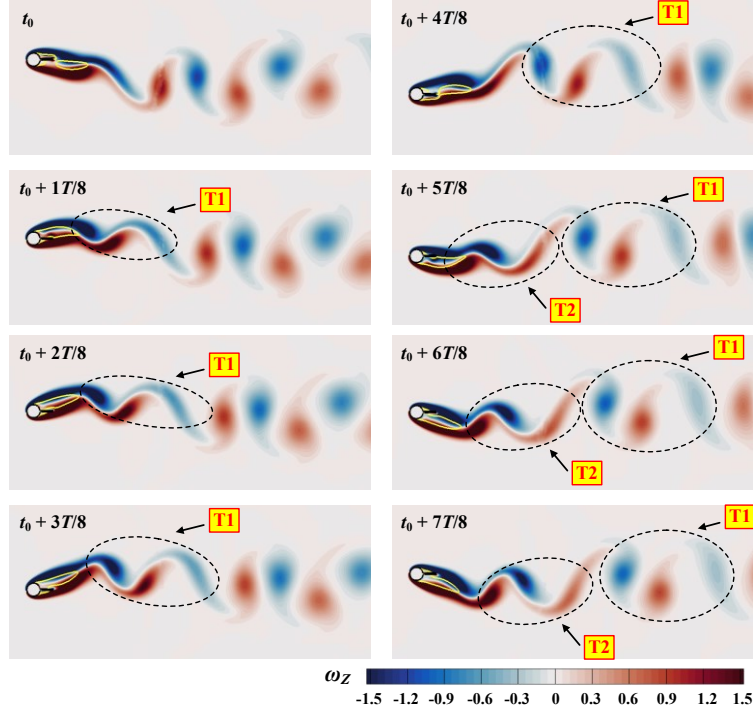


FIG. 16. Evolution of 2T mode within one vibration cycle starting from the maximum displacement ($U_y = 18$ and $U_\theta = 2$).

D. Understanding of rotary and vibrating augmentation

Vortex-induced vibration (VIV) and galloping are two typical FIV motions. As a self-excited nonlinear motion, VIV amplitudes are usually limited. Large amplitudes can be observed within a restricted Reynolds number range when the well-known “lock-in” phenomenon appears. In contrast, galloping represents a fluid instability phenomenon with larger or even uncontrollable amplitudes. Exposed to large-amplitude galloping over an extended period, structures are susceptible to stability and integrity issues, potentially shortening their lifespan. For this reason, it is imperative to discuss and understand the augmentation in the galloping region. This study has observed significant amplifications of rotation/vibration responses in the galloping-like region (Figs. 5–7). The mechanism underlying rotary augmentation is firstly elucidated through Figs. 17–19. Zhu *et al.*²⁸ suggested that the force torque exerted from ambient fluid including the pressure and shear stress can be used to explain rotation responses of a rotatable cylinder-plate. However, only the pressure exerted on the splitter plate needs to be considered, because (1) the torque from the wall shear stress on the splitter plate can be ignored because of the quite small arm with respect to the rotation center ($0.1D$ in this work); (2) the pressure acting on the cylinder surface cannot produce torque as the pressure is always perpendicular to the cylinder surface; and (3) the

shear stress on the cylinder can be also ignored as the stress distributions on the upper and lower surface are almost identical. Figure 17 compares the variations of pressure coefficient contours for two typical cases: the rotation-only case at $U_\theta = 18$ and the case considering both vibration and rotation responses at $U_y = 8$ and $U_\theta = 18$. It is clearly seen that the pressure distributions of the rotation-only case remain relatively consistent throughout one rotation period despite the regular vortex shedding behaviour. The high-pressure zone is situated around the front stagnation point due to the direct oncoming flow, while the low-pressure zone is proximate to the lower surface of the cylinder-plate. These pressure distributions result in continuous pressure differences, thereby inducing the clockwise rotation of the splitter plate. Pressure contours for the case considering both vibration and rotation responses in Fig. 17(b) significantly differ from those in Fig. 17(a). The position and extent of both high-pressure and low-pressure zone vary with time. At instant t_0 , where the cylinder-plate reaches to the position corresponding to the maximum angle, the high-pressure with a large control region is situated below the front stagnation point. At the same time, the lower surface of the cylinder-plate is entirely enveloped by the low-pressure zone, exhibiting a wide range. Consequently, the pressure difference across the splitter plate generates a driving force, propelling the cylinder-plate to rotate clockwise. From t_0 to $t_0+4T/8$ corresponding to the rotation process from maximum positive to maximum negative angle, the high-pressure zone gradually shifts to a position higher than the front stagnation point, while the control region initially decreases before returning to the same level as that at t_0 . A similar variation in pressure distributions is observed in the next half cycle of rotation, albeit in the opposite direction. Overall, the comparisons of pressure coefficients depicted in Fig. 17 indicate that the pressure zone of the cylinder-plate considering both vibration and rotation responses is substantially larger and temporally varying, resulting in significantly larger rotary angles compared with the rotation-only case.

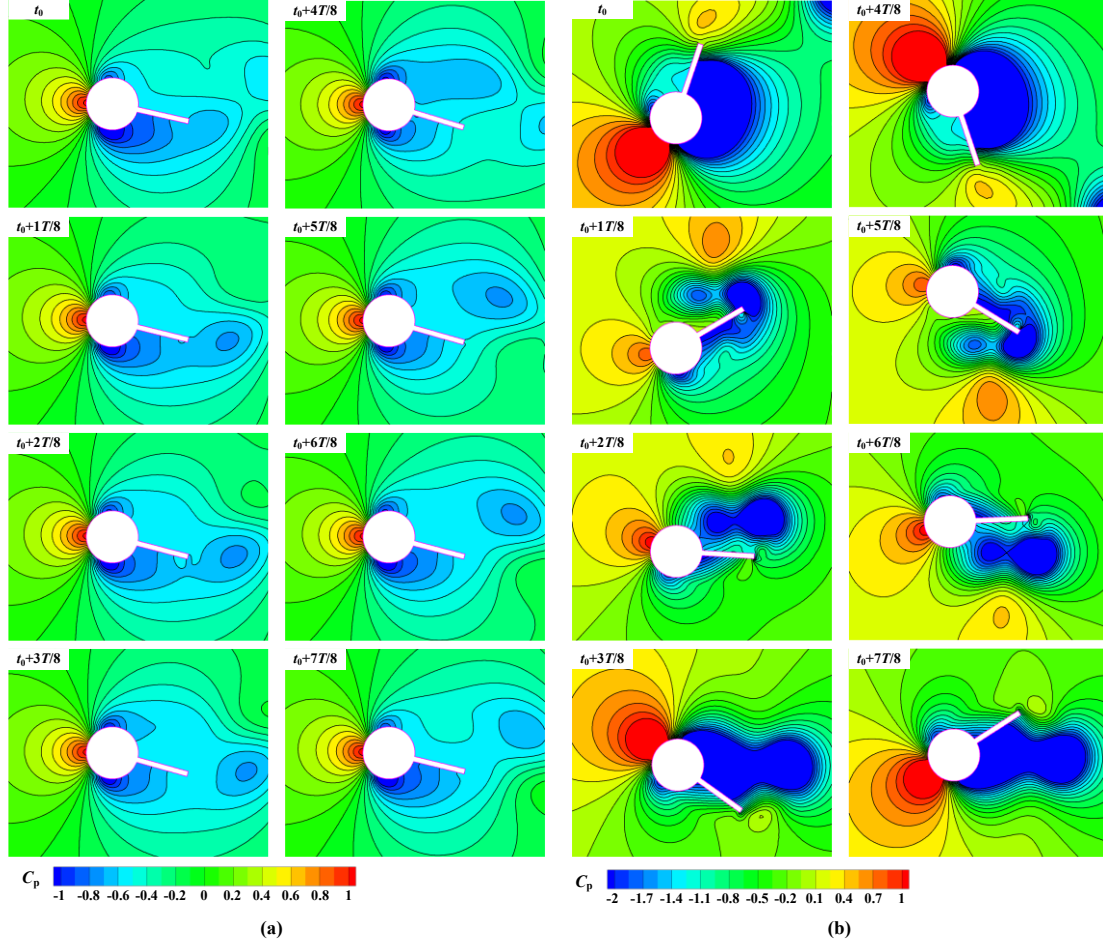


FIG. 17. Comparison of pressure coefficients in one rotation period between (a) the rotation-only case at $U_\theta = 18$ and (b) the case considering both vibration and rotation responses at $U_y = 8$ and $U_\theta = 18$.

To further understand the flow mechanism of rotary augmentation, a specific moment denoted as P in Fig. 18(a) is selected to analyze the forces acting on the cylinder-plate. At moment P in Fig. 18(a), the rotary angle θ is zero, while the displacement Y reaches its maximum negative value, indicating a phase difference of 90° between θ and Y . Additionally, the normalized moving velocity u_y/Y in the cross-flow direction is also equal to zero due to the 90° phase lag between u_y/Y and Y as depicted in Fig. 18(a). However, the accelerated velocity reaches to its maximum value because of the maximum slope of the u_y/Y curve at moment P, consequently resulting in the maximum inertia force. Figure 18(b) compares the driving force components between rotation-only case and the case considering both vibration and rotation responses. In both cases, a low pressure zone is observed near the lower side of the cylinder-plate when the vortex is shed from the lower surface of the circular cylinder. This pressure difference generates a torsional force,

causing the cylinder-plate to rotate clockwise. However, an extra force needs to be considered when both vibration and rotation are taken into consideration. As analyzed in Fig. 18(b), the direction of both the accelerated velocity and the inertia force F is upward, leading to a downward direction for the extra force acting on the splitter plate, consistent with the pressure difference direction. Consequently, the total torsional force for the case considering both vibration and rotation responses, comprising the pressure difference due to vortex shedding and the extra force due to relative motion, is significantly augmented (Fig. 19(a)), resulting in much greater rotary responses (Fig. 19(b)).

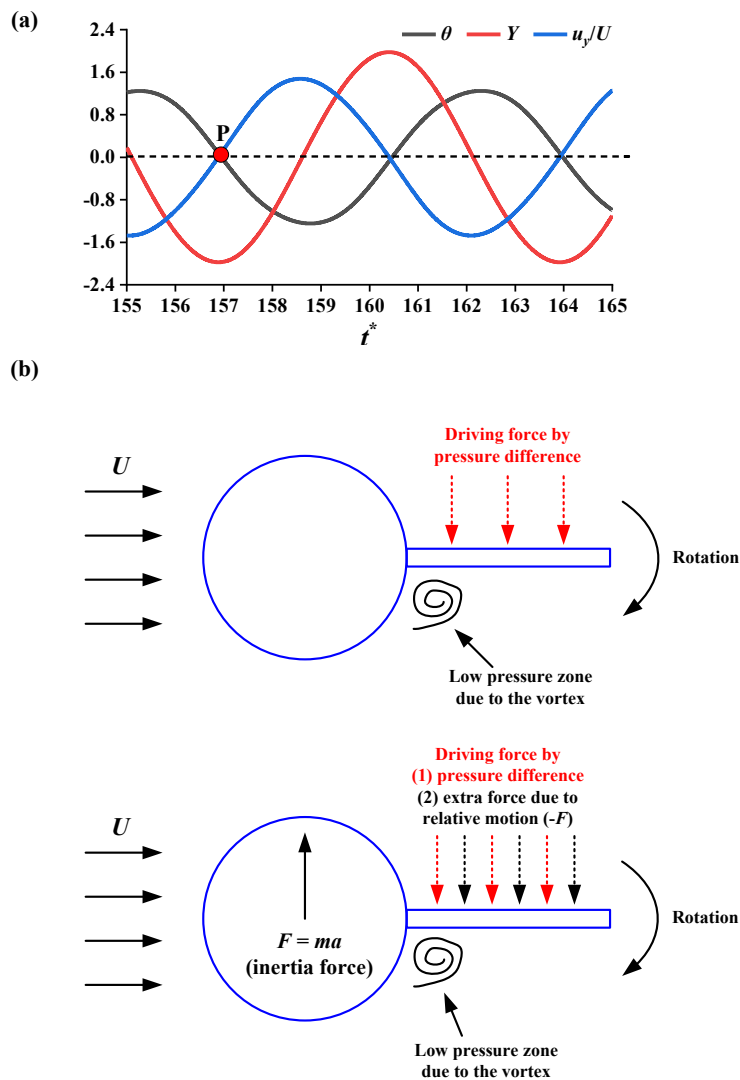


FIG. 18. (a) time-histories of rotary angle θ , displacement Y , and vibrating velocity u_y/U ; (b) components of driving force between rotation-only case and the case considering both vibration and rotation responses.

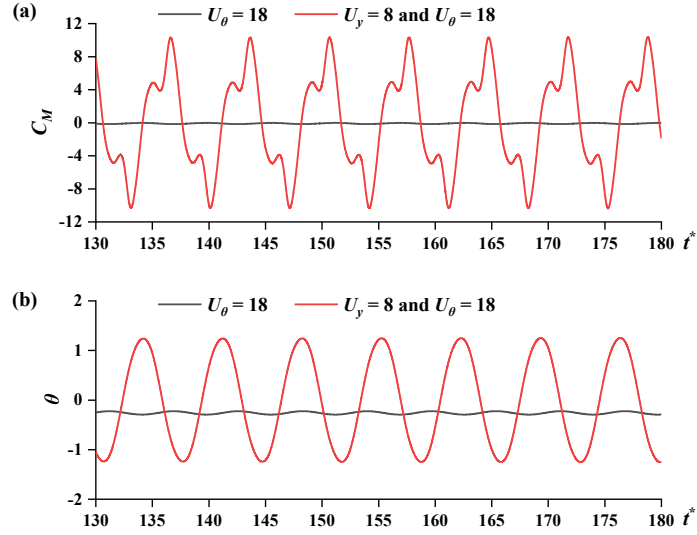


FIG. 19. Comparisons of (a) time histories of pitching moment coefficients and (b) rotary angles for the rotation-only case at $U_\theta = 18$ and the case considering both vibration and rotation responses at $U_y = 8$ and $U_\theta = 18$.

To understand the vibration augmentation, eight typical configurations of the cylinder-plate in one vibration period are presented in Fig. 20. Evidently, the projected area relative to the resultant velocity U^* remains constrained within the cylinder diameter D , indicating the persistent concealment of the splitter plate behind the circular cylinder and thereby maintaining a streamlined profile. This dynamic response underscores the cylinder-plate's capability to adapt its configuration with the objective of mitigating drag force and thus enhancing vibration.

In conclusion, for the cylinder-plate considering both vibration and rotation responses, rotary augmentations can be attributed to the introduction of an extra force stemming from the relative transverse motion, and the streamlined profile is responsible for the vibrating augmentation.

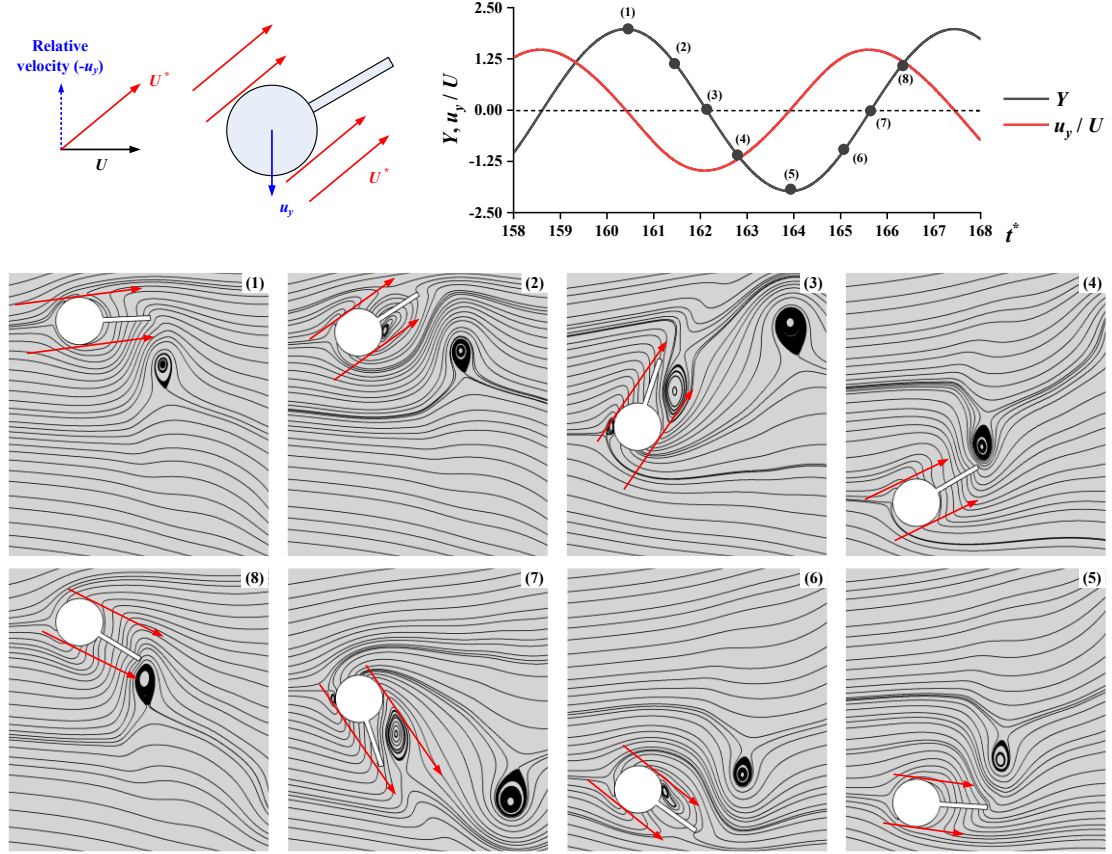


FIG. 20. Analysis of vibration responses at $U_y = 8$ and $U_\theta = 18$.

IV. CONCLUSIONS

In this work, two-dimensional numerical simulations were employed to investigate the role of cross-flow vibrations in the flow-induced rotations of an elastically mounted cylinder-plate system at a Reynolds number of 120. Comparative simulations were performed across a wide rotational reduced velocity range of $U_\theta = 2-18$ under varying vibrational reduced velocities of $U_y = 5, 8, 12,$ and 18 . The main conclusions drawn from this work are summarized below.

(1) The bifurcation region varies with both U_θ and U_y , which actually reflect the damping and stiffness effect. At low vibrational reduced velocities of $U_y = 5$ and 8 , no bifurcation phenomena are observed across the entire U_θ range. However, increasing U_y which effectively diminishes the influence of vibration oscillations will lead to evident bifurcation. The boundary between bifurcation and non-bifurcation region locates at $U_\theta = 12$ for both $U_y = 5$ and 8 . Within bifurcation region, the time-averaged rotary angle and displacement rise with the increasing U_θ . Furthermore, the variations of time-averaged values at larger U_y closely follow the trend observed in the rotation-only case, indicating a reduced influence of vibrational damping and stiffness.

(2) Variations of amplitudes and frequencies depict four distinct response modes:

vibration-dominated, rotation-dominated, augmentation (VIV-like), and augmentation (galloping-like) mode. Vibration-dominated mode, characterized by similar vibration amplitudes to those of the vibration-only case while nearly zero rotary amplitudes, appears at low U_θ . Following the vibration-dominated mode, the rotation-dominated mode is observed in the range of $U_\theta = 2.5-7$, $4.5-11$, and $4.5-18$ for $U_y = 8$, 12 , and 18 , respectively. In this mode, the rotation amplitudes approach those observed in the rotation-only scenario, whereas the vibration amplitudes tend towards zero. At $U_y = 5$, VIV-like mode appears after the vibration-dominated mode. The amplitudes of this mode are larger than those of pure rotation/vibration case, although showing a decreasing trend with increasing U_θ . Additionally, the frequencies basically follow a Strouhal law. Conversely, the galloping-like mode manifests as amplitudes rise sharply at the onset U_θ and grow continuously with U_θ . Furthermore, the non-dimensional frequencies deviate from the Strouhal line, being lower. This mode is observed in the range of $U_\theta = 7.5-18$ and $12-18$ for $U_y = 8$ and 12 , respectively.

(3) Phase angles between rotary angle and displacement exhibit a close relationship with response modes. In the VIV-like region, a phase angle of 180° is observed, while the galloping-like region is marked by a phase angle of 90° . Phase angles in rotation-dominated show a continuous decreasing trend. Significant increases in phase angles can be clearly observed during transitions between response modes, such as the shift from the vibration-dominated mode to the rotation-dominated mode, as well as the transition from the rotation-dominated mode to galloping-like mode. In contrast, phase angles at $U_y = 5$ vary smoothly, reflecting a shift from the vibration-dominated mode to the VIV-like mode.

(4) Vortex shedding modes are closely linked to response modes. In the rotation-dominated and VIV-like modes, the wake predominantly exhibits a 2S mode. Conversely, the vibration-dominated mode is characterized by a dominant 2T mode. In the galloping-like region, the wake patterns become more complex. At $U_y = 8$ where bifurcation is absent, the wake undergoes a sequence of 2S, $2S^*$, and 2P mode. In contrast, the bifurcation occurs at $U_y = 12$, resulting in asymmetrical wake flows and the appearance of P+S and 2P+S mode. The six distinctly different vortex shedding modes indicates the significant interaction between flow-induced vibration and flow-induced rotation.

(5) The mechanism behind rotary and vibrating augmentation is elucidated through

qualitative analyses. Compared with the rotation-only case, the high and low pressure zone around the cylinder-plate are substantially larger and vary with time, consequently leading to greater pressure differences and larger rotary angles. Further, qualitative analyses of components of the driving torsional force are conducted. For the rotation-only case, the torsional force originates from the pressure difference between two sides of the splitter plate, which is due to the vortex shedding behavior. In contrast, the total torsional force considering both vibration and rotation responses consists of the pressure difference due to vortex and the extra force due to the relative motion in the transverse direction. These two component forces share the same direction, resulting in greater rotary responses. The vibration augmentation is mainly attributed to a streamlined profile, where the splitter plate maintains its position rearward of the circular cylinder concerning the resultant velocity, devoid of direct interaction. The streamlined profile is helpful to reduce drag force and thus enhance vibration.

While valuable insights have been gained from current investigations, it's essential to acknowledge the limitations of this study and identify areas for future research. One notable limitation is the restriction to two-dimensional conditions, which may not fully capture the complexities of the flow dynamics in three-dimensional manner. Therefore, future studies could explore three-dimensional simulations to provide a more comprehensive understanding of the flow-induced responses. Additionally, the length of the splitter plate could influence the flow patterns and response characteristics. Investigating the effects of varying splitter plate lengths could offer valuable insights into the fluid-structure interaction phenomena. Furthermore, expanding the ranges of rotational and vibrational reduced velocity could provide a more thorough exploration of the system behavior. By studying a wider range of parameter values, we can better understand the transitional behaviors and identify critical thresholds for different response modes. In conclusion, future studies should aim to address these limitations by exploring three-dimensional conditions, investigating varying splitter plate lengths, and expanding the ranges of rotational and vibrational parameters. These efforts will contribute to a deeper understanding of flow-induced responses and improve the predictive capabilities of fluid-structure interaction models.

Acknowledgments

The research work was supported by National Natural Science Foundation of China (Nos.

51979238 and 52301338), Sichuan Science and Technology Program (Nos. 2023NSFSC1953 and 2023ZYD0140), and China Scholarship Council. The authors appreciate the support from the Offshore Oil and Gas Laboratory at Southwest Petroleum University.

References

- ¹A. Roshko, “On the wake and drag of bluff bodies,” *J. Aeronaut. Sci.* **22**, 124 (1955).
- ²Y. Bao, D. Zhou, and J. H. Tu, “Flow interference between a stationary cylinder and an elastically mounted cylinder arranged in proximity,” *J. Fluids Struct.* **27**, 1425–1446 (2011).
- ³C. J. Apelt and G. S. West, “The effects of wake splitter plates on bluff-body flow in the range $10^4 < R < 5 \times 10^4$. Part 2,” *J. Fluid Mech.* **71**, 145–160 (1975).
- ⁴Y. Qiu, Y. Sun, Y. Wu, and Y. Tamura, “Effects of splitter plates and Reynolds number on the aerodynamic loads acting on a circular cylinder,” *J. Wind Eng. Ind. Aerod.* **127**, 40–50 (2014).
- ⁵A. R. Ogunremi and D. Summer, “The effect of a splitter plate on the flow around a finite prism,” *J. Fluid. Struct.* **59**, 1–21 (2015).
- ⁶Y. Nakamura, “Vortex shedding from bluff bodies with splitter plates,” *J. Fluid. Struct.* **10**, 147–158 (1996).
- ⁷H. J. Zhu, G. M. Li, and J. L. Wang, “Flow-induced vibration of a circular cylinder with splitter plates placed upstream and downstream individually and simultaneously,” *Appl. Ocean Res.* **97**, 102084 (2020).
- ⁸J. C. Xu, M. Sen, and M. Gad-el-Hak, “Low-Reynolds number flow over a rotatable cylinder-splitter plate body,” *Phys. Fluids* **2**, 1925–1927 (1990).
- ⁹J. D. Crawford and E. Knobloch, “Symmetric and symmetry-breaking bifurcations in fluid dynamics,” *Annu. Rev. Fluid Mech.* **23**, 341–387 (1991).
- ¹⁰J. C. Xu, M. Sen, and M. Gad-el-Hak, “Dynamics of a rotatable cylinder with splitter plate in uniform flow,” *J. Fluids Struct.* **7**, 401–416 (1993).
- ¹¹J. M. Cimbalá and K. T. Chen, “Supercritical Reynolds number experiments on a freely rotatable cylinder-splitter plate body,” *Phys. Fluids* **6**, 2440 (1994).
- ¹²J. M. Cimbalá and S. Garg, “Flow in the wake of a freely rotatable cylinder with splitter plate,” *AIAA J.* **29**, 1001–1003 (1991).
- ¹³G. R. S. Assi, P. W. Bearman, and N. Kitney, “Low drag solutions for suppressing vortex-induced vibration of circular cylinder,” *J. Fluids Struct.* **25**, 666–675 (2009).
- ¹⁴F. Gu, J. S. Wang, X. Q. Qiao, and Z. Huang, “Pressure distribution, fluctuating forces and vortex shedding behavior of circular cylinder with rotatable splitter plates,” *J. Fluids Struct.* **28**, 263–278 (2012).
- ¹⁵T. Tang, H. J. Zhu, J. S. Wang, M. M. Alam, and J. Z. Song, “Flow-induced rotation modes and wake characteristics of a circular cylinder attached with a splitter plate at low Reynolds numbers,” *Ocean Eng.* **266**, 112823 (2022).
- ¹⁶L. Lu, X. L. Guo, G. Q. Tang, M. M. Liu, C. Q. Chen, and Z. H. Xie, “Numerical investigation of flow-induced rotary oscillation of circular cylinder with rigid splitter plate,” *Phys. Fluids* **28**, 093604 (2016).
- ¹⁷M. J. Zhang, X. Wang, and O. Øiseth, “Torsional vibration of a circular cylinder with an attached splitter plate in laminar flow,” *Ocean Eng.* **236**, 109514 (2021).

- ¹⁸G. R. S. Assi, P. W. Bearman, and M. A. Tognarelli, “On the stability of a free-to-rotate short-tail fairing and a splitter plate as suppressors of vortex-induced vibration,” *Ocean Eng.* **92**, 234–244 (2014).
- ¹⁹M. J. Zhang, O. Øiseth, and F. Y. Xu, “Laminar flow-induced vibration of a three-degree-of-freedom circular cylinder with an attached splitter plate,” *Phys. Fluids* **33**, 113605 (2021).
- ²⁰T. Tang, H. J. Zhu, Q. Xiao, Q. Y. Chen, J. W. Zhong, Y. M. Li, and T. M. Zhou, “Coupled responses of the flow-induced vibration and flow-induced rotation of a rigid cylinder-plate body,” *Ocean Eng.* **286**, 115709 (2023).
- ²¹M. R. Rastan, A. Sohankar, and M. M. Alam, “Flow and heat transfer across two inline cylinders: Effect of blockage, gap spacing, Reynolds number, and rotation direction,” *Int. J. Heat Mass Tran.* **174**, 121324 (2021).
- ²²H. J. Zhu, and Y. Gao, “Hydrokinetic energy harvesting from flow-induced vibration of a circular cylinder with two symmetrical fin-shaped strips.” *Energy*, **165**, 1259–1281 (2018).
- ²³T. Tang, H. J. Zhu, Q. Y. Chen, G. M. Li, and T. M. Zhou, “CFD analysis of flow-induced rotation of a circular cylinder with a detached rear splitter plate in laminar flow,” *Ocean Eng.* **266**, 112703 (2022).
- ²⁴T. Tang, H. J. Zhu, Q. Y. Chen, J. W. Zhong, and Y. Gao, “Dynamic response of a circular cylinder in the presence of a detached splitter plate: On the gap distance sensitivity,” *J. Fluids Struct.* **119**, 103888 (2023).
- ²⁵R. Govardhan, and C. H. K. Williamson, “Modes of vortex formation and frequency response of a freely vibrating cylinder,” *J. Fluid Mech.* **420**, 85–130 (2000).
- ²⁶H. J. Zhu, T. Tang, Y. Gao, T. M. Zhou, and J. L. Wang, “Flow-induced vibration of a trapezoidal cylinder placed at typical flow orientations,” *J. Fluids Struct.* **103**, 103291 (2021).
- ²⁷C. H. K. Williamson, and N. Jauvtis, “A high-amplitude 2T mode of vortex-induced vibration for a light body in XY motion,” *Eur. J. Mech. B Fluid*, **23**, 107–114 (2004).
- ²⁸H. J. Zhu, T. Tang, M. M. Alam, J. Z. Song, and T. M. Zhou, “Flow-induced rotation of a circular cylinder with a detached splitter plate and its bifurcation behavior,” *Appl. Ocean Res.* **122**, 103150 (2022).